Geophysical Research Letters

RESEARCH LETTER
10.1029/2025GL117560

Urban Basin Structure Imaging in Northern Los Angeles From Ambient Noise Differential Adjoint Tomography

Zhanwen Li[1], **Xin Liu**[1], **Xi Wang**[1], **and Lina Gao**[1]

[1]Department of Earth and Planetary Sciences, The University of Hong Kong, Hong Kong SAR, China

Key Points:

- We apply differential adjoint tomography based on ambient noise data to a dense linear array in northern Los Angeles
- Our tomography results reveal possible fluid migration related to Fontana Seismicity and detailed basin structures
- We use a subregion-wise optimization strategy to enhance the convergence of iterative tomographic inversion due to uneven data coverage

Supporting Information:

Supporting Information may be found in the online version of this article.

Correspondence to:

X. Liu,
liuxine@hku.hk

Citation:

Li, Z., Liu, X., Wang, X., & Gao, L. (2025). Urban basin structure imaging in northern Los Angeles from ambient noise differential adjoint tomography. *Geophysical Research Letters*, *52*, e2025GL117560. https://doi.org/10.1029/2025GL117560

Received 12 JUN 2025
Accepted 21 NOV 2025

Abstract We employ differential adjoint tomography to suppress the effects of uneven noise sources and image the upper crust S wave velocity structure of San Gabriel Basin, Chino Basin and San Bernardino Basin in the northern Los Angeles. A Sequential Subdomain Inversion strategy is implemented to address regional imbalance of sensitivity kernel coverage and improve resolution in the region with suboptimal data coverage. Our results align well with known structures and reveal some undiscussed details in this region. Beyond delineating upper crustal structure, we analyzed the relationship between velocity anomalies and regional seismicity. Diffuse low-velocity anomalies detected at the Fontana Seismicity region provide evidence for fluid migration. The high-velocity channel within the San Jose Fault zone indicates that the fault acts as a water barrier. We also identified a concentrated low-velocity anomaly between 0.8 and 4 km depth beneath Puddingstone Reservoir, potentially indicating groundwater seepage.

Plain Language Summary Sedimentary basin complex in northern Los Angeles exhibits intricate stress field and fault structure resulting from prolonged tectonic movements. A detailed velocity structure of the region aids in study of seismic mechanism and assessment of regional seismic hazard. We extracted high-precision travel time data from a linear array of stations recording seismic ambient noise and employed new optimization strategies to enhance the resolution of the velocity structure images. Our results recovered high-precision structure of upper crust and revealed groundwater movements at the Fontana Seismicity region and Puddingstone Reservoir. The results demonstrated a strong correlation between velocity structure and regional seismicity.

1. Introduction

The San Gabriel Basin, Chino Basin and San Bernardino Basin are sedimentary basins situated at the northern edge of the Peninsular Range, adjacent to the southern edge of the central Transverse Range. The convergent tectonics of the Transverse Range and strike-slip motion of the Peninsular Range have created a complex stress field within this region along with multiple active faults (Hauksson, 1990).

An accurate basin structure model is important for seismic hazard assessment (Tanimoto, 1990). During earthquakes, seismic waves can be trapped and amplified within the sedimentary basin, thus leading to magnified ground motion effects. Integrating original extensive oil-exploratory data and seismic reflection data, Southern California Earthquake Center Unified Community Velocity Model (CVM) could provide reference of geological structure in this region (Kohler et al., 2003; Shaw et al., 2015). However, due to lack of accurate constraints in the northern basin complex, current CVMS model is considered to underestimate the ground motion effects induced by earthquakes around San Andreas Fault (Denolle et al., 2014).

To address the seismic data gap in the northern basins of Los Angeles, the Basin Amplification Seismic Investigation (BASIN) (Clayton et al., 2019) project deploying dense 2D seismic station arrays was conducted across this region. Data utilized in this research were from the longest linear station array SB1, which spans about 81 km from west to east (Figure 1). It comprises 237 Fairfield ZLAND 3C units with standard 5 Hz 3 component geophones, with an average spacing of ~330 m. This linear array starts from the Monterey Hills in the west, sequentially traversing the San Gabriel Basin, San Jose Hills, Chino Basin, and extends to the northwest of the San Bernardino Basin. Utilizing BASIN data, methods such as receiver function and ambient noise interferometry have been employed to map basin depth and Moho discontinuity (Ghose et al., 2023; Liu et al., 2018; Wang et al., 2021).

Based on assumption of fully diffuse noise field, Empirical Green's Function (EGF) derived from ambient seismic noise interferometry represents unit impulse response between a station pair. Adjoint tomography iteratively

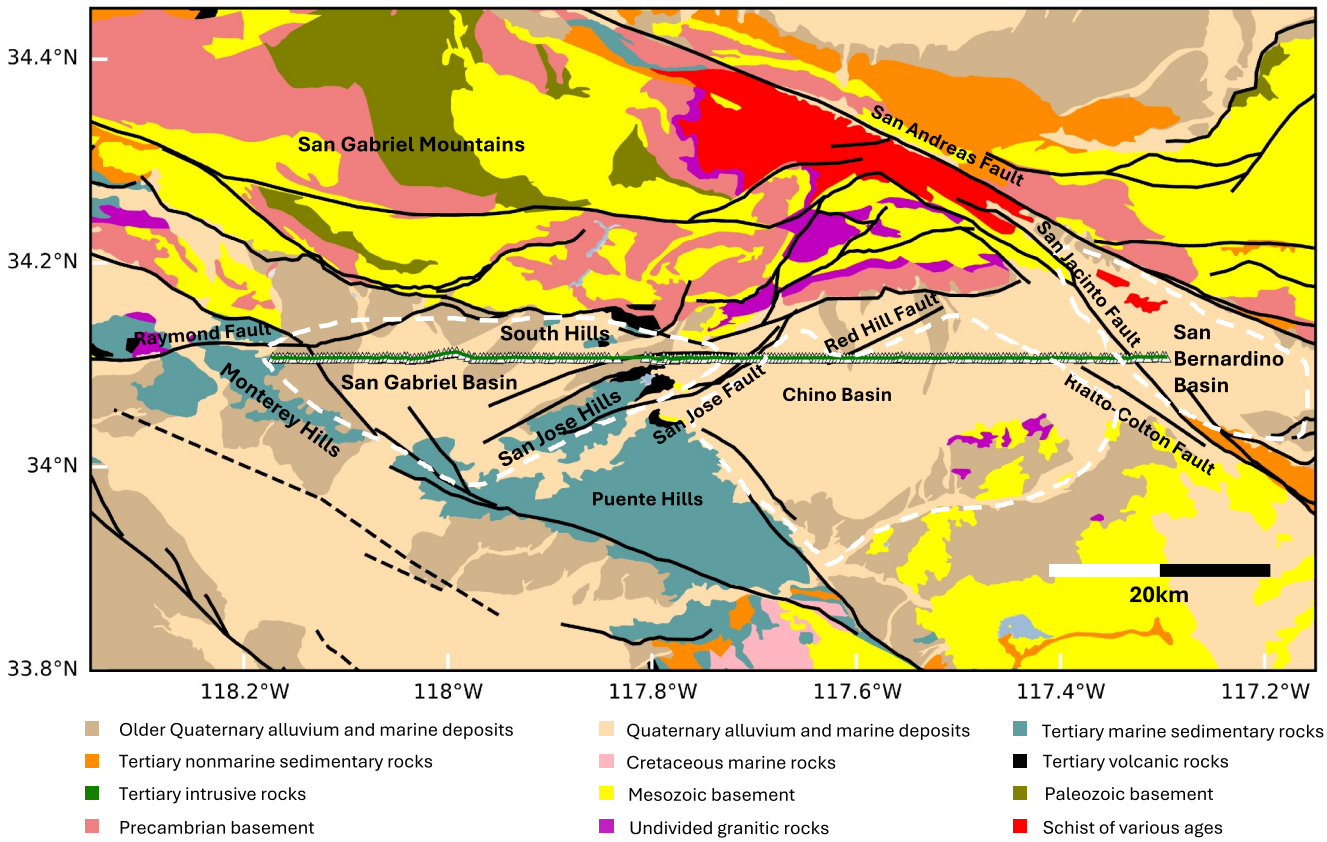

Figure 1. Map of the northern Los Angeles basins (Jennings et al., 1977) and configuration of SB1 array. The white triangles, interconnected by a green line, represent the Fairfield ZLAND 3c seismometers along the SB1 array. Black lines are fault locations based on CFM 5.2 model. The white dashed lines delineate the boundaries of the San Gabriel Basin, Chino Basin and San Bernardino Basin, respectively.

updates the model by sensitivity kernels (gradient of data misfit function) calculated from adjoint method (Liu et al., 2023; Tromp et al., 2005), and is effective in interpreting broadband earthquake and EGF data. However, in practice seismic noise is rarely diffuse and uniform. As a result, EGF cannot converge to actual Green's function but introduce systematic bias into ambient noise tomography results (Fichtner, 2015; X. Liu, 2020; Sager et al., 2018; Tromp et al., 2010). To address this problem, we employ differential adjoint tomography here combining differential time kernel (Chen et al., 2022; Chen et al., 2023; de Vos et al., 2013; Yan et al., 2024; Yuan et al., 2016) with ambient seismic noise tomography. This method could effectively eliminate sensitivity near noise sources, thereby maintaining the robustness of results even amidst uncertainties in source distribution.

In this study, we use ambient noise differential adjoint tomography to obtain SH wave velocity structure of northern Los Angeles basins. The Love wave EGF data we utilized were derived from stacking TT (transverse-transverse) component data of SB1 array for 1 month. We proposed a Sequential Subdomain Inversion strategy to improve low-resolution in the Chino Basin and San Jose Hills region caused by uneven sensitivity kernel coverage. Our model identifies several velocity anomalies matching local geological units and reveals a low-velocity patch corresponding to the Fontana Seismicity.

2. Methodology and Data Processing

In this section, we summarize the workflow for ambient noise differential adjoint tomography using data from a linear station array. Love waves are utilized in this research as they are conveniently extracted from transverse-transverse component. This workflow can be transferred to Rayleigh waves in future research.

2.1. Data Processing and Initial Model

We apply cross-correlation to 1-month data filtered between 0.1 and 0.3 Hz from November to December 2019 to ensure the data is not affected by anthropogenic noise above 1 Hz (Díaz et al., 2017; Shapiro et al., 2005). The continuous seismic recording is divided into 200s segments with 50s gaps. We assume that data segments within each day follow similar noise statistics (Liu et al., 2016), and 50s gap is to make sure neighboring segments are not correlated. Segments whose cross-spectrum deviates much from the median value (4 times median absolute deviation) are excluded from stacked cross correlations to suppress small seismic events and urban traffic noise. Our study area is located in northern Los Angeles near the west coast of North America and is imaged mainly by seismic noise generated from the Pacific Ocean. The energy of causal part of noise cross correlation is substantially higher than the anti-causal part (Figure S1 in Supporting Information S1), indicating stronger noise sources from the west coast.

Quality of tomography highly depends on the initial model. Following the standard procedure of Frequency Time Analysis (FTAN) (Bensen et al., 2007), we obtain the phase slowness between each station pair in various narrow frequency bands for fundamental mode wave. Then a linear inversion approach is applied to calculate dispersion curves of the discretized region model with a grid size of 200 m × 200 m. Finally, we apply SURF96 software to perform phase velocity inversion (Herrmann, 2013), integrating CVMS model as the initial model to incorporate extra geological constraints such as seismic reflection and borehole data. The result of phase velocity inversion is used as the initial model for ambient noise differential adjoint tomography.

2.2. Ambient Seismic Noise Differential Adjoint Tomography

Adjoint tomography utilizes adjoint method to efficiently compute gradients with respect to a specific misfit function, such as travel time differences between observed and synthetic waveforms. These gradients are used to iteratively optimize the model parameters. If the ambient noise field deviates from the uniform distribution, the discrepancy between synthetic and observed waveforms will be excessive to affect travel time misfit measurements (Fichtner, 2015; Tromp et al., 2010; Yuan et al., 2016). Such challenges are prevalent in ambient noise tomography as the noise field is generally not diffuse (Cupillard & Capdeville, 2010). Therefore, sensitivity kernels calculated from conventional travel time misfit measurements may not be able to accurately update the model.

To address this issue, we introduce a differential travel time kernel for ambient noise tomography constructed by station triplets (X. Liu, 2020; Liu et al., 2023). One station in the triplet acts as a virtual source (VS), and the sensitivity kernel of differential time between the VS and the other two closely spaced receivers is defined as "one-triplet kernel." The inter-station distance between the closely spaced receivers is less than 25% of their average distance to the VS to ensure maximum overlap of Fresnel zones from the VS to each receiver. The one-triplet kernel effectively cancels the sensitivity of the overlapping area and thus reduces the source signature (Figure S2 in Supporting Information S1). In the SB1 linear array, each station can serve as a VS whose sensitivity kernel combines multiple one-triplet kernel associated with it. To ensure accuracy, for each VS we only use one-triplet kernels corresponding to high SNR (SNR > 10) differential travel time measurements (Liu et al., 2016). The calculation process for sensitivity kernels is briefly reviewed in Text S1 of Supporting Information S1.

2.3. Subregion Wise Optimization

A misfit function for inverse problems may not be strictly convex, and it may have many local minima that hinder our ability to find out the optimal velocity model. We apply multi-scale inversion and subregion wise optimization to improve the convergence of iterative schemes towards a physically meaningful global minimum (Fichtner, 2011).

Based on quality of ambient noise observation, we first use low-frequency data (0.1–0.2 Hz) to perform inversion for large-scale features within the region, followed by refinement of smaller-scale and shallow part using high-frequency data (0.2–0.3 Hz). Due to the degradation of signal SNR as it travels from west to east, the number of applicable One-triplet kernel of virtual sources (VSs) exhibits regional variations (Figure 2a). The sensitivity kernel density in the western subregion generated by eastern VSs, is higher than that in the eastern subregion. The kernel coverage is notably sparse in the central subregion due to the limited number of one-triplet kernels that satisfy the requirement of sufficient VS-to-receiver distances for reliable travel time measurements (Figure 2a).

10.1029/2025GL117560

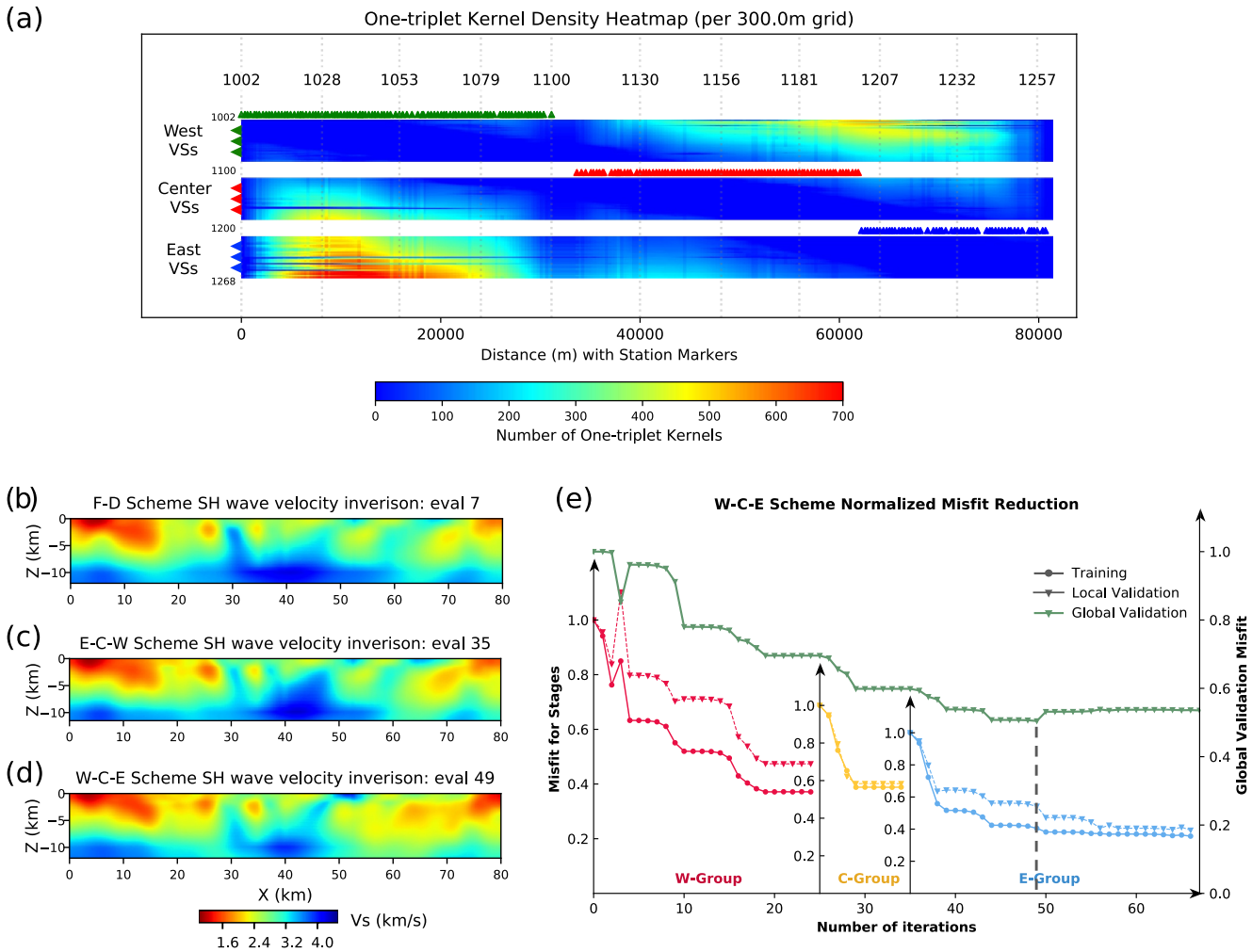

Figure 2. Differential sensitivity kernel coverage and tomography results under different schemes. (a) Station triplet differential kernel coverage for West Virtual Sources (VSs), Center VSs and East VSs. VS grouping method and their distributions are illustrated by distinct color markers. Each heatmap section represents one VS group with corresponding locations of individual VSs. The grid spacing is 300 m for the coverage figure. Colorbar represents the cumulative count of one-triplet kernels in each grid cell. (b, c, d) SH wave inversion results from low frequency differential adjoint tomography for depth between 0 and 12 km for F-D scheme, E-C-W scheme and W-C-E scheme. $X = 0$ km denotes the westernmost of the station array. For W-C-E scheme, the result is of 49th iteration, before overfitting is observed. (e) W-C-E scheme Normalized Misfit Reduction. Left y-axis indicate training misfit, marked by circle, and local validation misfit, marked by triangle. Right y-axis indicates global validation misfit. The misfit reduction curves for each round are confined to their respective iteration ranges, while that for global validation is continuously defined across all iterations.

The imbalance between subregions is pronounced that if all VS sensitivity kernels are simultaneously inverted, the subregions with sparse sensitivity will undergo slow updates and their structural characteristics will be obscured. Figure 2b shows this full-domain inversion result, and a faster evolution of structure on the west side overshadowed the relatively slower structural changes on the east side, causing the inversion trapped in local minimum.

To address this imbalance, we divided all VSs into 3 groups based on their sensitivity kernel coverage: the West group, Center group and East group, corresponding to their relative positions along the linear array (Figure 2a). A sequential optimization strategy was adopted that the inversion process is divided into three rounds, with each round only using a single VS group data. We compared the results of two inversion schemes with different sequential orders: the West-Center-East (WCE) scheme (Figure 2d) and the East-Center-West (ECW) scheme (Figure 2c). Additionally, we present the results of the full-domain scheme result for comparison (Figure 2b).

We follow the method proposed by Liu et al. (2023), utilizing independent VSs as validation set to prevent overfitting. We adopted two types of validation sets: global validation and local validation. Global validation set

is sampled from the entire domain and monitors the entire inversion process. The size of global validation set should be sufficient to preserve the main features of the model while retaining sufficient training data. Therefore, we selected 15 VSs with a mean spacing of 5.8 km as the global validation set. As shown in Figure S4 of Supporting Information S1, the sensitivity kernel generated from the global validation set could capture similar model features as that from the training set, thereby validating the rationale of the validation set selection. Local validation set is to calibrate the inversion process of the subregions, it is chosen from the global validation set and is in corresponding round's VS group. These two approaches enhance the robustness of our inversion by ensuring model reliability at both global and regional scales.

3. Results

We present the results of SH wave velocity structure on low-frequency data 0.1–0.2 Hz under the F-D, E-C-W and W-C-E scheme respectively (Figures 2b–2d). In the west subregion corresponding to the San Gabriel Basin, the results of 3 schemes are similar. In the center and east part, E-C-W and W-C-E schemes yield higher resolution structures and exhibit differences in the low-velocity anomaly distribution beneath the Chino Basin.

Normalized misfit function (Figure 2e) of W-C-E scheme and that of E-C-W and F-D scheme (Figures S5a and S5b in Supporting Information S1) show consistent decreasing trend but with varying convergence efficiency. Misfit curves in each round are independent and thus normalized separately, as shown by the left y-axes corresponding to each round in the figure. The global validation set is normalized separately, corresponding to right y-axis and it starts to decrease from baseline of 1.0. Misfit reduction for W-C-E scheme experiences several plateau stages, indicating the algorithm's continued exploration in the model space and search for better solutions (Figure 2e). Occasional spurious fluctuations can be attributed to line search method when determining optimal step length (Honkela et al., 2010). Misfit of local validation set slightly exceeds the training set and gradually converge to training set. Misfit of the global validation set decreases slowly because the model is only partially updated at each round. Notably, global validation set reaches its optimal at the 49th iteration, indicating compromised global accuracy as the model overfitted subregional features afterwards. Thus, we take the velocity parameter at the 49th iteration as the result of this scheme. Misfit for E-C-W scheme (Figure S5b in Supporting Information S1) decreases rapidly in the first 5 iterations. This implies the algorithm has found the dominating characteristics of the model early in the inversion process. However, this premature convergence (Honkela et al., 2010) could lead to the model getting stuck in local optima close to the initial point and sabotage the model's further improvement. Overfitting occurs at the 35th iteration for E-C-W scheme. The final misfit reductions for the three schemes are 41.9% for F-D scheme, 48.7% for E-C-W scheme and 49.6% for W-C-E scheme respectively.

Based on the low-frequency band tomography result under W-C-E scheme, we use 0.2–0.3 Hz data to perform another round of differential adjoint tomography under the same scheme (Figure S6b in Supporting Information S1). Despite the expected shallow and small-scale updates in the model, it exhibits pronounced oscillatory features and strong side lobe energy. Additionally, high-frequency data doesn't bring significant changes to the model. Therefore, we adopt the low-frequency band W-C-E scheme result as our best-fitting model (Figure 2d).

A checkerboard test was done to demonstrate the depth and lateral resolution of our differential adjoint tomography algorithm. We generated synthetic data using 7% checkerboard anomalies superimposed on a layered model resembling initial model in this study. Two consecutive rounds of inversion were performed using data filtered by two specific frequency bands: 0.05–0.18 Hz and 0.15–0.23 Hz. Figure S7 in Supporting Information S1 displays good lateral and vertical resolution in this region although some degradation at the model edges is observed due to suboptimal sensitivity coverage.

We establish a west–east X-axis along the SB1 station array, with the westernmost station as the origin. The region spanning from the East Montebello Fault at about $X \sim 4$ km to the western edge of the San Jose Hills and the South Hills at $X \sim 30$ km corresponds to the San Gabriel Basin. This region features a broad and deep low-velocity zone beneath the surface. An approximate 1.8 km/s isovelocity contour separates the upper low-velocity zone from the underlying section. It starts at approximately 2 km depth at $X = 0$ km in Raymond basin, gradually deepening towards the east. The 1.8 km/s contour reaches its maximum depth of 4.8 km at $X \sim 15$ km and bends upward at $X \sim 17$ km before it continues to deepen eastwards. This high-velocity zone spans a range from $X \sim 17$ to ~ 25 km and indicates a significant shallowing of the basin depth near the San Gabriel River. The low-velocity region

terminates at $X \sim 28$ km, near the easternmost edge of the basin. The lowest velocity is observed at surface at $X \sim 3$ km. Below the depth of 5 km, the SH wave velocity decrease from west to east.

The region bounded west by the San Jose Fault at $X \sim 44$ km and to the east by the Rialto Colton Fault at $X \sim 74$ km corresponds to the Chino Basin. Compared with the sharp vertical velocity gradient in the San Gabriel Basin, the SH wave velocity structure observed in this region is overall uniform, ranging approximately between 2.5 and 3.1 km/s. Beneath the basin bottom, there are some low-velocity anomalies and a high-velocity anomaly. The high-velocity channel originated at $X \sim 45$ km, extending upward and eastward and surfacing at $X \sim 50$ km. Low-velocity anomalies are diffusely distributed within a depth range of 2–8 km between $X \sim 60$ and 75 km.

The region between $X \sim 30$ and 44 km represents that SB1 array passes through the channel linking two relatively stable basins. The array borders the northeastern corner of the San Jose Hills and lies less than 1 km from the southern foot of San Gabriel Mountains in the north. In the region, an approximate 3.2 km/s isovelocity contour bends downward at $X \sim 34$ km. The high-velocity zone below is connected to the high-velocity channel at the western edge of the Chino Basin. In addition, at $X \sim 34$ km corresponding to northern corner of San Jose Hills, a concentrated 2 km wide low-velocity anomaly is located at depths ranging from 0.8 to 4 km.

The easternmost part of our velocity map shows the northwestern section of the San Bernardino Basin. Within this region, the shallow part above 4 km depth exhibits low velocity. Below 4 km depth, velocity decreases slowly.

4. Discussion

Combining the high-quality noise cross correlations achieved through SNR selection and the robustness of differential adjoint tomography to noise sources, our model reveals various structural details (Figure 3). Seismic energy released from 1920 till 2025 within 5 km on either side is projected onto the profile (Figure 3a). By integrating velocity anomalies from our findings with seismicity, we find good agreements between Fontana Seismicity and a low-velocity anomaly possibly connected to fluid migration. Our findings also offer new constraints on local geological structures when combined with previous studies.

The Northern Los Angeles Basin Complex is situated at the junction of the Transverse Range and Peninsular Range, exhibiting north–south contraction, east–west extension and strike-slip features (Walls et al., 1998). This region comprises two relatively stable basin units connected by an active fold belt (Yeats, 2004). The area has undergone multiple phases of subsidence and uplift, with alternating marine and terrestrial sedimentation, as well as periods of active volcanism (Bjorklund et al., 2002). The complex stress regime and Quaternary faulting have resulted in loosely consolidated strata, which facilitate groundwater movement.

4.1. Groundwater Migration and Fontana Seismicity

The Chino Basin is a half-graben located in the northern part of the Perris block. The basement of the basin is primarily composed of Peninsular Range type igneous and metamorphic crystalline rock. Hundreds of meters thick Quaternary water-bearing sediments are on the surface of the basin. Influenced by deposition of ancestral Santa Ana River, the porosity of sediments in the Chino Basin is lower in the central area and higher on both sides, with the central porosity being as low as 3%–6%. The groundwater outflow is restricted by the presence of surrounding faults such as San Jose Fault and Red Hill Fault (Wildermuth Environmental, Inc, 2003).

As the Chino Basin is about 1–1.5 km deep (Ghose et al., 2023), this region (Figure 3a) features roughly uniform velocity for the basement complex (X between 44 and 74 km). We find new diffuse low-velocity anomalies (X between 60 and 74 km) in the eastern part of the basin at moderate depths. These anomalies correspond to a broad area centered around Fontana Seismicity and are less than 7 km deep (Figures 3a and 3b). Based on the BASIN data, Nardoni and Persaud (2024) identified high absorption anomalies which were interpreted as fluid-filled rocks. By analyzing the spatial-temporal changes in the earthquake sequence during this period, they inferred that the basement is highly fractured with ongoing deformation and groundwater might be a secondary cause of the diffuse seismicity. Our results further suggest the low-velocity zone is a combination of both fractured structure and fluid migration. Such correspondence between low-velocity anomaly and water-bearing layers has been found before (Lee, 2002; Liu et al., 2023). The Perris Block (Figure 1) has a basement primarily composed of plutonic rocks and constitutes a stable and unfaulted crustal unit. North–south contraction is accommodated by crustal-scale conjugate faults along its margins, with no measurements of slip rate supporting existence of internal major faults (Walls et al., 1998). Based on the orientation of this seismic swarm, we propose that they are

10.1029/2025GL117560

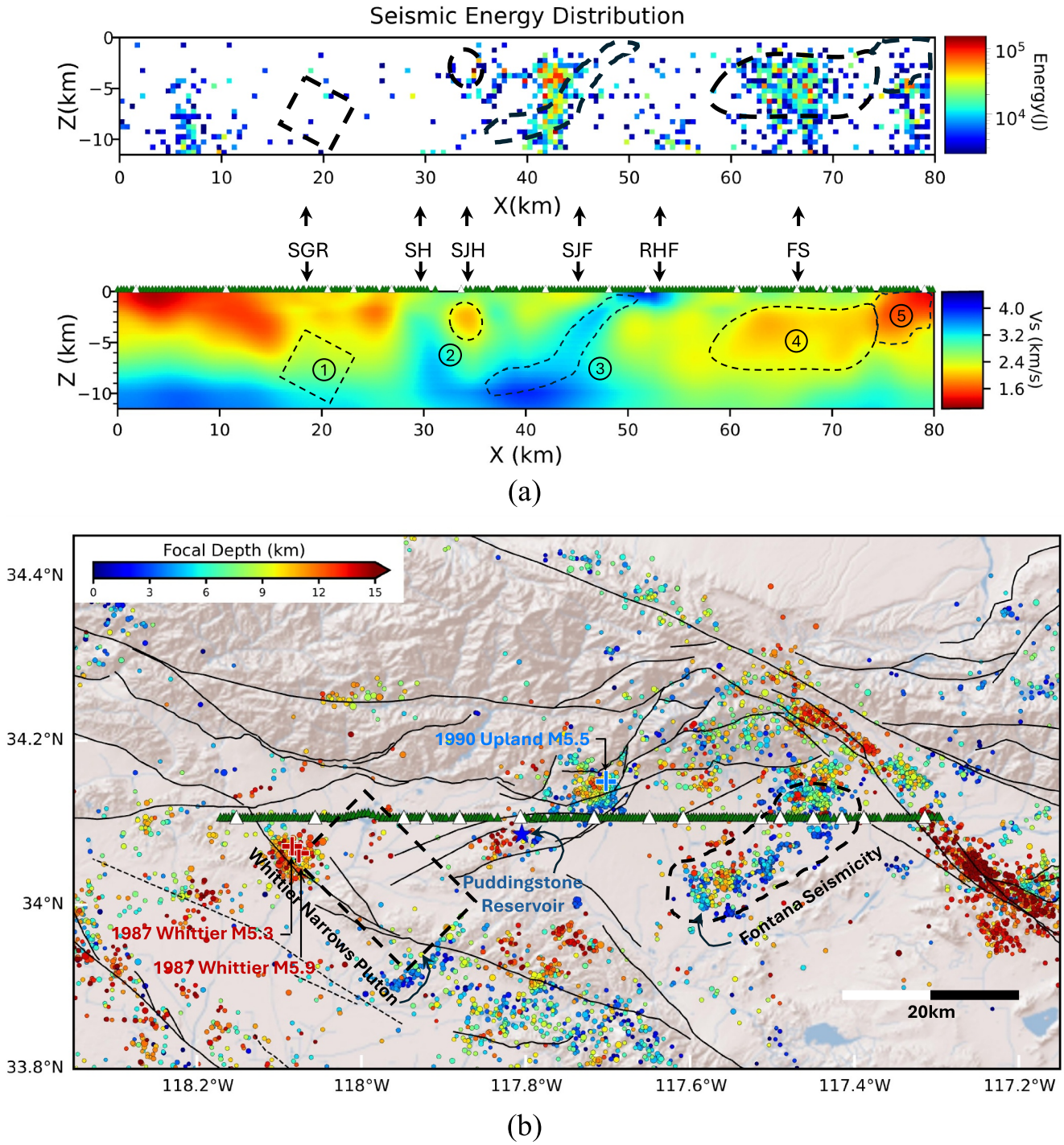

Figure 3. SH Wave Velocity Structure, Seismic energy distribution and Associated Geological Features in northern Los Angeles basins. (a) Velocity structure and corresponding geological interpretations. Zones marked by numbers are observed velocity anomalies. Seismic energy distribution is the projection of a collection of M2-M5 seismic events from 1920 till 2025 within 5 km on either side of the station array on the profile according to their hypocenter locations and depths. Magnitudes are local magnitudes (M_L) and were converted to energy (J) using the empirical relation $\log E = 1.5\,M_L + 4.8$. SGR, San Gabriel River; SH, South Hills; SJH, San Jose Hills; SJF, San Jose Fault; RHF, Red-Hill Fault; FS, Fontana Seismicity. Bottom portion shows terrain map with outline of SB1 array. Green triangles represent 222 stations for training set, white triangles represent 15 stations for validation set. (b) Map showing seismic events from 01/01/1975 to 15/07/2024, with focal depths ranging from 0 to 15 km and magnitudes from M2 to M5 (U.S. Geological Survey, 2025). The color of data points denotes focal depth. The larger the size of the data point, the greater the magnitude. Three significant earthquakes are marked by a cross symbol, which are 1987 Whittier Narrow Earthquakes (M5.9 and M5.3), and 1990 Upland Earthquake (M5.5). Green and white triangles represent stations. The blue star marks Puddingstone Reservoir. Black dashed lines mark Whittier Narrows Pluton inferred by Bjorklund (Bjorklund et al., 2002) and Fontana Seismicity zone.

distributed along a reactivated joint system (Hauksson et al., 2019). Within these structural weak planes, elevated differential stress enables fluid-induced effective normal stress reduction to locally exceed the Coulomb failure threshold and trigger rupture cascades. This mechanism aligns with minor left-lateral slip motion of Fontana Seismicity (Margaret L. Gooding, 2007). Because the seismicity swarms are not connected to major faults and are confined to shallow depths (<5 km), the seismic energy of this zone is limited.

Another low-velocity anomaly is observed, ranging from approximately 0.8 to 4 km in depth, corresponding to the northeastern corner of San Jose Hills and just below the Puddingstone Reservoir. Built in 1920s, the Puddingstone Reservoir is an artificial lake that spans approximately 1 km^2. Applying satellite radar interferometry time series analysis, Lanari et al. (2004) observed ground surface uplift around Puddingstone in 1998, 1999 and 2000 which was led by influx of water into the aquifer. A lack of microseismicity within the low-velocity anomaly is observed (Figure 3b). We propose the existence of groundwater seepage along a network of fractures and pores in volcanic rocks which modulate seismicity in this area. As the north–south contraction is distributed across the surrounding fault system, strain energy accumulation is lower within fractured rock mass. Reduction of effective normal stress caused by pore pressure elevation is insufficient to induce rupture. Additionally, the lubrication of contact surfaces by fluids significantly lowers the frictional coefficient. These combined mechanisms facilitate aseismic deformation along the fracture network. Subsequently, tectonic stress is transferred to adjacent areas. This stress redistribution, at least, partially drives peripheral microseismicity. Similarly, Scuderi and Collettini (2016) suggest that increase of fluid pressure promotes stable sliding within fracture zones, thereby releasing regional tectonic stress and reducing the likelihood of large earthquakes.

4.2. San Gabriel Basin and Rigid Intrusion-Induced Stress Locking

The San Gabriel Basin is situated to the south of the San Gabriel Mountains, with the left-lateral Raymond Fault to its west (Jones et al., 1990). The basin is encircled on the southwestern and southern side by Repetto, Montebello and Puente Hills. To the east lies the San Jose Hills and a series of faults. The basement primarily consists of Pre-Tertiary San Gabriel Mountain gneissoid rock (Yerkes et al., 1965). Overlying the basement, the superjacent rocks are consolidated sedimentary rocks from the Pliocene and Pleistocene periods (Yeats, 2004). Additionally, Miocene volcanic deposits are exclusively present east of the San Gabriel River and outcrop in the South Hills and northeastern San Jose Hills. The surface of the basin is covered by loosely consolidated Quaternary deposits, in the form of alluvial fans.

The low-velocity zone at the surface in $X < 4$ km (Figure 3a) may correlate with the outcrops of Upper Miocene rock in the Monterey Hills located west of the basin. The composition consists of poorly sorted friable sandstone, siltstone and shale, which are overlain by sandstones of various grain sizes, resulting in high porosity and low seismic wave velocities (Yerkes et al., 1965). Extending eastward along the SB1, the basement reaches its maximum depth on the west bank of the San Gabriel River. This finding agrees with a previous basin model (Villa et al., 2023), which suggests an asymmetric bowl-shaped basin. An increase in seismic velocity east of the San Gabriel River supports the existence of volcanic rock and Duarte Conglomerate (Yeats, 2004). Proceeding eastward, an obvious velocity contrast is observed, corresponding to the western boundary of the South Hills. Velocity contrast may be related to the boundary of Glendora volcanics outcrop in the South Hills and San Jose Hills, and it could be associated with more compressed state in the fold belt.

Previous P-wave model (Bjorklund et al., 2002) identified a high-velocity anomaly on the east of the Whittier Narrows, corresponding to one of three plutons (Yerkes et al., 1965) associated with volcanic activity during Miocene. Their finding aligns with the high-velocity anomaly around $X \sim 20$ km in our figure, leading to our inference that this could be a shallow expression of the pluton (Figures 3a and 3b). In contrast to their depth estimate, our study reveals that the northern margin of Whittier Narrows pluton may extend as shallow as 4 km and affect the shape of the San Gabriel Basin. A seismic gap related to pluton region is observed as shown in Figures 3a and 3b. The pluton acts as a rigid buttress within the regional tectonic framework, exhibiting two key mechanical effects. First, the pluton impedes fault propagation and controls the spatial distribution of seismicity. Second, it modulates regional stress field. Concentrated seismic energy release at the pluton margins is likely attributed to strain accumulation and abrupt release process driven by its obstruction to fault slip. Thus, seismic energy accumulation in this zone warrants careful consideration.

4.3. Basin-Margin Fold Belts and Faults

Connecting the San Gabriel Basin and Chino Basin, the San Jose Hills transitional zone includes the San Jose Hills, the South Hills, and the southern foot of San Gabriel Mountains. The region hosts several northeast-trending Quaternary faults that have potential to produce reverse-fault earthquakes. Known faults include the strike-slip Walnut Creek Fault and Indian Hill Fault associated with the 1988 and 1989 Upland earthquakes and the reverse San Jose Fault.

The San Jose Hills transitional zone features distinct relatively high S wave velocity (Figure 3a), implying shallow basement burial due to absence of Plio-Pleistocene strata and regional compression. A series of minor earthquakes (M2-M5) along the faults at depth of 0–15 km since 1975 suggests active tectonics (Figure 3b).

High-velocity channel penetrating the basement to the surface coincides with the San Jose Fault and Red Hill Fault. The north-dipping San Jose Fault is an effective groundwater barrier. Within this region, volcanic rocks are interbedded with consolidated sediments, and the fault system is under a transpressional stress regime. Therefore, breccias are likely to exist within the fault system. Under conditions of elevated pressure and temperature in depth, the combined effect of shearing and cementation might facilitate the development of dense fault gouge. We therefore propose that this high-velocity channel is related to high-density, low-permeability layers within the fault system which cause groundwater level difference across the fault. Furthermore, a strong concentration of seismic energy is observed above the high-velocity channel (Figure 3a), supporting thrust fault characteristics of San Jose Fault zone. This seismicity concentration can be attributed to shear failure in the rocks of the hanging wall due to intense friction during its upward thrust.

This linear array extends eastward into the northwest side of the San Bernardino Basin, a wedge-shaped sedimentary basin constrained by the San Jacinto Fault and San Andreas Fault. Although resolution test (Figure S7 in Supporting Information S1) indicates suboptimal accuracy due to limited sensitivity coverage, the observed shallow low velocities contrast notably with deeper high velocities. This may be attributed to San Jacinto Fault traversing this region and causing fracturing of strata, resulting in slower shallow velocities. Pressure at depth leads to closure of fractures, thus exhibiting higher velocity.

Conflict of Interest

The authors declare no conflicts of interest relevant to this study.

Data Availability Statement

All the broadband seismic waveform data used in this study are available on IRIS DMC in 2024 (http://service.iris.edu/ph5ws/). CVMS model used in this study is available from UCVM framework (Small et al., 2017) (https://doi.org/10.1785/0220170082). Seismic station array SB1 used in this study are available from IRIS (Persaud, 2019).

Acknowledgments
We thank the editor Germán Prieto, the associate editor and three anonymous reviewers for their helpful comments in improving the manuscript. This project is funded by Research Grants Council (RGC) in Hong Kong (Project 17304924 and 27302323) and National Natural Science Foundation of China (Project U1939203). The final S wave velocity model is stored on Dataverse (https://doi.org/10.7910/DVN/XLX9F8). We thank the Basin Amplification Seismic Investigation (BASIN) project participants and supporting institutions for data acquisition and for making the data openly available.

References

Bensen, G. D., Ritzwoller, M. H., Barmin, M. P., Levshin, A. L., Lin, F., Moschetti, M. P., et al. (2007). Processing seismic ambient noise data to obtain reliable broad-band surface wave dispersion measurements. *Geophysical Journal International*, *169*(3), 1239–1260. https://doi.org/10.1111/j.1365-246X.2007.03374.x

Bjorklund, T., Burke, K., Zhou, H., & Yeats, R. S. (2002). Miocene rifting in the Los Angeles basin: Evidence from the Puente Hills half-Graben, volcanic rocks, and P-wave tomography. *Geology*, *30*(5), 451–454. https://doi.org/10.1130/0091-7613(2002)030<0451:MRITLA>2.0.CO;2

Chen, G., Chen, J., Tape, C., Wu, H., & Tong, P. (2023). Double-difference adjoint tomography of the crust and uppermost mantle beneath Alaska. *Journal of Geophysical Research: Solid Earth*, *128*(1), e2022JB025168. https://doi.org/10.1029/2022JB025168

Chen, J., Chen, G., Wu, H., Yao, J., & Tong, P. (2022). Adjoint tomography of Northeast Japan revealed by common-source double-difference travel-time data. *Seismological Research Letters*, *93*(3), 1835–1851. https://doi.org/10.1785/0220210317

Clayton, R., Persaud, P., Denolle, M., & Polet, J. (2019). Exposing Los Angeles's shaky geologic underbelly. *Eos*, *100*. https://doi.org/10.1029/2019EO135099

Cupillard, P., & Capdeville, Y. (2010). On the amplitude of surface waves obtained by noise correlation and the capability to recover the attenuation: A numerical approach. *Geophysical Journal International*, *181*(3), 1687–1700. https://doi.org/10.1111/j.1365-246X.2010.04586.x

Denolle, M. A., Dunham, E. M., Prieto, G. A., & Beroza, G. C. (2014). Strong ground motion prediction using virtual earthquakes. *Science*, *343*(6169), 399–403. https://doi.org/10.1126/science.1245678

de Vos, D., Paulssen, H., & Fichtner, A. (2013). Finite-frequency sensitivity kernels for two-station surface wave measurements. *Geophysical Journal International*, *194*(2), 1042–1049. https://doi.org/10.1093/gji/ggt144

Díaz, J., Ruiz, M., Sánchez-Pastor, P. S., & Romero, P. (2017). Urban seismology: On the origin of Earth vibrations within a city. *Scientific Reports*, *7*(1), 15296. https://doi.org/10.1038/s41598-017-15499-y

Fichtner, A. (2011). *Full seismic waveform modelling and inversion*. Springer Berlin Heidelberg. https://doi.org/10.1007/978-3-642-15807-0
Fichtner, A. (2015). Source-structure trade-offs in ambient noise correlations. *Geophysical Journal International*, *202*(1), 678–694. https://doi.org/10.1093/gji/ggv182
Ghose, R., Persaud, P., & Clayton, R. W. (2023). Basin structure for earthquake ground motion estimates in urban Los Angeles mapped with nodal receiver functions. *Geosciences*, *13*(11), 320. https://doi.org/10.3390/geosciences13110320
Hauksson, E. (1990). Earthquakes, faulting, and stress in the Los Angeles basin. *Journal of Geophysical Research*, *95*(B10), 15365–15394. https://doi.org/10.1029/JB095iB10p15365
Hauksson, E., Ross, Z. E., & Cochran, E. (2019). Slow-growing and extended-duration seismicity swarms: Reactivating joints or foliations in the Cahuilla Valley Pluton, central peninsular ranges, Southern California. *Journal of Geophysical Research: Solid Earth*, *124*(4), 3933–3949. https://doi.org/10.1029/2019JB017494
Herrmann, R. B. (2013). Computer programs in seismology: An evolving tool for instruction and research. *Seismological Research Letters*, *84*(6), 1081–1088. https://doi.org/10.1785/0220110096
Honkela, A., Raiko, T., Kuusela, M., Tornio, M., & Karhunen, J. (2010). Approximate Riemannian conjugate gradient learning for fixed-form Variational Bayes. *Journal of Machine Learning Research*, *11*, 3235–3268.
Jennings, C. W., Strand, R. G., Rogers, T. H., Boylan, R. T., Moar, R. R., & Switzer, R. A. (1977). *Geologic map of California*. California Division of Mines and Geology. Retrieved from https://mrdata.usgs.gov/geology/state/kml/cageol.kml
Jones, L. M., Sieh, K. E., Hauksson, E., & Hutton, L. K. (1990). The 3 December 1988 Pasadena, California earthquake: Evidence for strike-slip motion on the Raymond fault. *Bulletin of the Seismological Society of America*, *80*(2), 474–482. https://doi.org/10.1785/BSSA0800020474
Kohler, M. D., Magistrale, H., & Clayton, R. W. (2003). Mantle heterogeneities and the SCEC reference three-dimensional seismic velocity model version 3. *Bulletin of the Seismological Society of America*, *93*(2), 757–774. https://doi.org/10.1785/0120020017
Lanari, R., Lundgren, P., Manzo, M., & Casu, F. (2004). Satellite radar interferometry time series analysis of surface deformation for Los Angeles, California. *Geophysical Research Letters*, *31*(23). https://doi.org/10.1029/2004GL021294
Lee, M. W. (2002). Biot–Gassmann theory for velocities of gas hydrate-bearing sediments. *Geophysics*, *67*(6), 1711–1719. https://doi.org/10.1190/1.1527072
Liu, G., Persaud, P., & Clayton, R. W. (2018). Structure of the Northern Los Angeles basins revealed in teleseismic receiver functions from short-term nodal seismic arrays. *Seismological Research Letters*, *89*(5), 1680–1689. https://doi.org/10.1785/0220180071
Liu, X. (2020). Finite-frequency sensitivity kernels for seismic noise interferometry based on differential time measurements. *Journal of Geophysical Research: Solid Earth*, *125*(4), e2019JB018932. https://doi.org/10.1029/2019JB018932
Liu, X., Ben-Zion, Y., & Zigone, D. (2016). Frequency domain analysis of errors in cross-correlations of ambient seismic noise. *Geophysical Journal International*, *207*(3), 1630–1652. https://doi.org/10.1093/gji/ggw361
Liu, X., Beroza, G. C., & Li, H. (2023). Ambient noise differential adjoint tomography reveals fluid-bearing rocks near active faults in Los Angeles. *Nature Communications*, *14*(1), 6873. https://doi.org/10.1038/s41467-023-42536-4
Margaret, L. G. (2007). *Seismic hazards of the Fontana trend*. Manchester Metropolitan University.
Nardoni, C., & Persaud, P. (2024). Evidence for faulting and fluid-driven earthquake processes from seismic attenuation variations beneath metropolitan Los Angeles. *Scientific Reports*, *14*(1), 17595. https://doi.org/10.1038/s41598-024-67872-3
Persaud, P. (2019). Los Angeles basin seismic experiment [Dataset]. *International Federation of Digital Seismograph Networks*. https://doi.org/10.7914/SN/6J_2019
Sager, K., Ermert, L., Boehm, C., & Fichtner, A. (2018). Towards full waveform ambient noise inversion. *Geophysical Journal International*, *212*(1), 566–590. https://doi.org/10.1093/gji/ggx429
Scuderi, M. M., & Collettini, C. (2016). The role of fluid pressure in induced vs. triggered seismicity: Insights from rock deformation experiments on carbonates. *Scientific Reports*, *6*(1), 24852. https://doi.org/10.1038/srep24852
Shapiro, N. M., Campillo, M., Stehly, L., & Ritzwoller, M. H. (2005). High-resolution surface-wave tomography from ambient seismic noise. *Science*, *307*(5715), 1615–1618. https://doi.org/10.1126/science.1108339
Shaw, J. H., Plesch, A., Tape, C., Suess, M. P., Jordan, T. H., Ely, G., et al. (2015). Unified structural representation of the southern California crust and upper mantle. *Earth and Planetary Science Letters*, *415*, 1–15. https://doi.org/10.1016/j.epsl.2015.01.016
Small, P., Gill, D., Maechling, P. J., Taborda, R., Callaghan, S., Jordan, T. H., et al. (2017). The SCEC unified community velocity model software framework. *Seismological Research Letters*, *88*(6), 1539–1552. https://doi.org/10.1785/0220170082
Tanimoto, T. (1990). Modelling curved surface wave paths: Membrane surface wave synthetics. *Geophysical Journal International*, *102*(1), 89–100. https://doi.org/10.1111/j.1365-246X.1990.tb00532.x
Tromp, J., Luo, Y., Hanasoge, S., & Peter, D. (2010). Noise cross-correlation sensitivity kernels: Noise cross-correlation sensitivity kernels. *Geophysical Journal International*, *183*(2), 791–819. https://doi.org/10.1111/j.1365-246X.2010.04721.x
Tromp, J., Tape, C., & Liu, Q. (2005). Seismic tomography, adjoint methods, time reversal and banana-doughnut kernels. *Geophysical Journal International*, *160*(1), 195–216. https://doi.org/10.1111/j.1365-246X.2004.02453.x
U.S. Geological Survey. (2025). Earthquake Hazards Program (EHP) [Dataset]. Retrieved from https://earthquake.usgs.gov/earthquakes/
Villa, V., Li, Y., Clayton, R. W., & Persaud, P. (2023). Three-dimensional basin depth map of the northern Los Angeles basins from gravity and seismic measurements. *Journal of Geophysical Research: Solid Earth*, *128*(7), e2022JB025425. https://doi.org/10.1029/2022JB025425
Walls, C., Rockwell, T., Mueller, K., Bock, Y., Williams, S., Pfanner, J., et al. (1998). Escape tectonics in the Los Angeles metropolitan region and implications for seismic risk. *Nature*, *394*(6691), 356–360. https://doi.org/10.1038/28590
Wang, X., Zhan, Z., Zhong, M., Persaud, P., & Clayton, R. W. (2021). Urban basin structure imaging based on dense arrays and Bayesian array-based coherent receiver functions. *Journal of Geophysical Research: Solid Earth*, *126*(9), e2021JB022279. https://doi.org/10.1029/2021JB022279
Wildermuth Environmental, Inc. (2003). Optimum basin management program Chino Basin dry-year yield program modeling report. Retrieved from https://www.cbwm.org/docs/engdocs/dryyearyieldreport/Text/Text%20-%20Section%202.pdf
Yan, M., Yao, H., Lei, T., Luo, S., & Feng, J. (2024). Linear array double difference adjoint ambient noise tomography of the central Tanlu fault zone, Eastern China. *Journal of Geophysical Research: Solid Earth*, *129*(7), e2024JB028791. https://doi.org/10.1029/2024JB028791
Yeats, R. (2004). Tectonics of the San Gabriel basin and surroundings, southern California. *Geological Society of America Bulletin*, *116*(9), 1158. https://doi.org/10.1130/B25346.1
Yerkes, R. F., McCulloh, T. H., Schoellhamer, J. E., & Vedder, J. G. (1965). *Geology of the Los Angeles Basin, California — An introduction (No. 420- A)*. Professional Paper. U.S. Geological Survey. https://doi.org/10.3133/pp420A
Yuan, Y. O., Simons, F. J., & Tromp, J. (2016). Double-difference adjoint seismic tomography. *Geophysical Journal International*, *206*(3), 1599–1618. https://doi.org/10.1093/gji/ggw233